Research Article

Premysl Marsik*, Roberto de Andrés Prada, Andreana Daniil and Christian Bernhard

Ellipsometry study of the infrared-active phonon modes in strained SrMnO₃ thin films

Abstract: We performed infrared and time-domain tera-hertz spectroscopic ellipsometry measurements of thin films of the perovskite antiferromagnetic insulator $SrMnO_3$ that were grown by pulsed laser deposition (PLD) on $LaAlO_3$, $SrLaGaO_4$, and LSAT substrates which yield an epitaxial strain ranging from −0.3 to 1.7%. Taking these thin films as a representative example, we discuss the strategies for analyzing the ellipsometry spectra and extracting the information about the thin film dielectric response that can be equally applied to a variety of oxide based thin films and heterostructures. In particular, for the room temperature spectra we show that the three infrared-active phonon modes of the cubic perovskite structure of $SrMnO_3$ undergo the expected softening with increasing tensile strain. For the $SrMnO_3$ film on $SrLaGaO_4$, we find that the low-energy (TO1) phonon mode reveals anomalous temperature dependence in the vicinity of the Néel temperature of about 170 K that signifies a strong spin-phonon coupling. For the $SrMnO_3$ film on LSAT, we identify some irreversible changes of the infrared ellipsometry spectra that occur as the sample is heated to elevated temperature up to 560 K. These changes of the ellipsometry spectra have been attributed to a partial oxygen loss of the $SrMnO_3$ thin film since they can be reverted with a post annealing treatment under high oxygen pressure.

*Corresponding author: Premysl Marsik, Department of Physics, University of Fribourg, Chemin du Musee 3, 1700, Fribourg, Switzerland, E-mail: premysl.marsik@unifr.ch. https://orcid.org/0000-0001-9759-8325
Roberto de Andrés Prada and Christian Bernhard, Department of Physics, University of Fribourg, Fribourg, Switzerland, E-mail: roberto.deandres@gmail.com (R. de Andrés Prada), christian.bernhard@unifr.ch (C. Bernhard). https://orcid.org/0000-0002-9957-3487 (C. Bernhard)
Andreana Daniil, Department of Physics, University of Fribourg, Fribourg, Switzerland; and CENTREDOC, Rue Jaquet-Droz 1, 2002 Neuchâtel, Switzerland, E-mail: andreanadaniil@gmail.com

1 Introduction

Spectroscopic ellipsometry is a well-established technique for the investigation of thin films. In its most common instance, it deals with optical properties in the near infrared to ultraviolet range of films with thicknesses on the order of the wavelength. It is commonly used in fundamental and applied research, as well as in standard process control tools in microelectronic and related industries. Ellipsometry with long wavelength radiation in the mid-infrared, far infrared, and THz ranges is hampered by several experimental complications, but as a research field, it has been steadily progressing for several decades [1, 2]. The recent availability of commercial infrared ellipsometers certainly has brought more attention to the long wavelength range, where the optical response of a film/substrate system approaches the ultrathin film limit ($d << \lambda$), with a dominating response from the substrate and a weak contribution of the film that is quasilinear as a function of its thickness.

Transition metal oxides with strongly correlated electrons, like the cuprate high-temperature superconductors and the colossal magneto-resistive or multiferroic manganates, have been thoroughly studied by optical techniques in their bulk form [3–5]. Due to the small energy scales of the phenomena involved, the experiments often require cryogenics and a focus on the low energy infrared and THz ranges. For such materials, the thin film paradigm opens routes for designing novel functionalities by applying epitaxial strain [6], combining materials into multilayered heterostructures and exploring interface phenomena [7, 8]. While the oxide thin film field is broad and many different experimental techniques are employed, optical studies of these systems are quite rare – especially those taking advantage of infrared ellipsometry. In this manuscript, we aim to present infrared and THz ellipsometry as viable tools for investigating strained oxide thin films with the manganate $SrMnO_3$ as specific example. We also discuss the analysis and interpretation of

the ellipsometric spectra at the ultrathin film limit, in the presence of a strong phonon response of the substrate.

SrMnO$_3$ in its bulk form is a G-type antiferromagnetic insulator, with T_N = 233 K, which crystalizes in a cubic perovskite structure with the lattice parameter a = 3.805 Å [9]. By changing the chemical pressure with the substitution of the larger Ba atoms (Sr$_{1-x}$Ba$_x$MnO$_3$), the material approaches a displacive ferroelectric transition that is manifested by the softening of a low energy phonon. The latter has a peculiar temperature dependence that has been observed by infrared reflectivity and interpreted in terms of spin-phonon coupling [10–12].

Theoretical studies predicted that the ferroelectric transition can also be induced in SrMnO$_3$ (or in similar CaMnO$_3$) thin films via epitaxial strain [13, 14]. Due to the existing spin-phonon coupling in these materials [15, 16], with sufficient strain it should be even possible to change the ground state from an antiferromagnetic to a ferromagnetic one. If achieved, such a system would represent an interesting multiferroic, with the ferroelectricity originating from the displacement of the magnetic Mn^{4+} ions, and with a strong coupling between the ferroic orders [17]. Such intriguing predictions from first principles calculations have inspired an avalanche of experimental work and indeed, the incipient ferroelectricity and polar order was soon confirmed for thin films that are subjected to a tensile strain of about 2% [18, 19]. Eventually, a highly strained state (4%) was required for a 10 nm thick SrMnO$_3$ film to exhibit a long-range ferroelectric order with a remanent polarization of ~55 μC/cm^2 [20]. In that study, the ultrathin film was grown in the form of a sandwich structure, with the film being capped by a layer of the same material as the substrate (DyScO$_3$) to protect the SrMnO$_3$ film from degradation. However, the sample remained antiferromagnetic, i.e. no ferromagnetic component was observed.

Meanwhile, it was found that the strain in SrMnO$_3$ tends to be compensated by a change in stoichiometry and the formation of oxygen vacancies [21, 22]. A parallel route has also been followed by combining the epitaxial strain with chemical pressure in the form of Sr$_{1-x}$Ba$_x$MnO$_3$ films [23, 24].

The infrared spectra can provide global and reliable information about the quality and strain state of such films. The expected displacive ferroelectric transition gives rise to a softening of the low frequency phonon [25], and also to anomalies of other infrared-active phonons that can provide valuable insight to the structural changes. The above cited work of Goian et al. [24] is to our best knowledge the only attempt to determine the infrared optical response of such films.

2 Experiment

Epitaxial SrMnO$_3$ (SMO) films with a thickness of 30 nm were grown by pulsed laser deposition (PLD) on commercial $10 \times 10 \times 0.5$ mm^3 oxide substrates that were chosen for matching the lattice parameter of bulk SrMnO$_3$, a = 3.805 Å, with an added strain. LaAlO$_3$ (001) provides a small compressive strain of –0.3%. SrLaGaO$_4$ (001) a tensile strain of +1.1% and (La$_{0.3}$Sr$_{0.7}$) (Al$_{0.65}$Ta$_{0.35}$)O$_3$ (or LSAT) a tensile strain of +1.7%. The SMO films have been capped with 2 nm of LaAlO$_3$ that acts as a protective layer. The samples were deposited at 825 °C in a O$_2$ partial pressure of 0.12 mbar, with a laser fluence of 2 J/cm^2 and a repetition rate of 2 Hz. The growth was monitored with *in-situ* reflection high electron diffraction (RHEED). After deposition, the samples were cooled to 700 °C at a rate of 10 °C/min, while the oxygen partial pressure was gradually increased to 1 bar. Subsequently, the temperature was further decreased at the rate of 30 °C/min to 485 °C, where it was kept for 1 h. Finally, the samples were cooled to room temperature at a rate of 30 °C/min and removed from the PLD chamber. For one of the samples, a separate high-pressure chamber was used to perform an additional O$_2$ annealing at 300 °C and 5 bar pressure for a duration of 3 h.

The structural quality of the films was confirmed by ex-situ XRD measurements with a Rigaku SmartLab diffractometer. The THz and IR ellipsometry experiments have been performed with home-built setups that were already previously used for the study of such complex oxide systems [26–28]. The infrared ellipsometer is based on a vacuum system that is attached to a Bruker IFS 133 spectrometer and uses a 1.2 K He-cooled bolometer as detector and polyethylene-supported wire grids as polarizers. It is operated in rotating analyzer (RAE) mode in polarizer-sample-analyzer (PSA) configuration with optional static compensator (PCSA) based on the total internal reflection of Silicon prism. The instrument is similar to the one presented in ref. [29]. The low frequency part of the spectra was measured with a home-built time-domain THz ellipsometer, based on Menlo Systems C-Fiber 780 nm pulsed laser, with photoconductive antennas as emitter and detector, and free-standing wire grids as polarizers. Details of the instrument configuration can be found in ref. [26]. Each of the polarizers is a tandem of high-quality wire grids, providing very high degree of polarization. Thanks to the amplitude- and phase-sensitive time-domain spectroscopic technique, the ellipsometer can be operated in simple RAE mode, without the need of static or rotating compensators. The analysis of the raw spectral data needs to be modified for the case of polarization selective detector (antenna) [30, 31]. Both the IR and THz ellipsometers are equipped with He-flow cryostats from Cryovac that enable measurements in the range from 5 to 300 K. The infrared ellipsometer can also be equipped with a heating stage which enables measurements under vacuum condition for temperatures up to 750 K. For the Visible/NIR/UV part of the spectrum we used a near-infrared extended Woollam VASE instrument. The spectroscopic data in the form of ellipsometric angles Ψ and Δ exhibit good match between the THz and FIR instruments. Subsequently, the data are analyzed using in-house built software.

We did not determine the magnetic properties of our samples; however, similar films were studied by Maurel et al. [32] using the low-energy muon spin rotation (μSR) technique. They observed a transition to an antiferromagnetic state at 224 K for a SrMnO$_3$ film grown on

LaAlO₃ and at 171 K on LSAT. For both films, the AF transition was quite a bit broader than the one in the bulk material at 227 K.

3 Theory

The optical response of a thin film on a substrate (ambient/film/substrate) is a cornerstone topic in spectroscopic ellipsometry. The forward problem can be solved exactly using well-known transfer matrix formalism [33]. The inversion of the data, i.e. the interpretation of measured ellipsometric spectra in terms of some model is often discussed for the case of a thin film in the visible range with $d \approx \lambda$.

The situation is quite different for the infrared response of a thin film that is grown on an oxide substrate with a perovskite structure. Here the wavelength exceeds by far the thickness of the film which for PLD grown epitaxial films is typically on the order of several tens of nanometers ($d \ll \lambda$). Moreover, the oxide substrates tend to have rather strong infrared active phonon modes which dominate infrared response, whereas the thin film only gives rise to small modifications of the spectra. In terms of model parameter estimates, the statistical correlation between the film thickness and its optical properties becomes very high. With the exception of some special cases, an independent determination of both parameters thus becomes impossible, as will be discussed below. Therefore, one typically has to assume that film thickness is known *a-priori* (target thickness of PLD checked by *in-situ* RHEED, determined by ex-situ XRR, or by ellipsometry in visible/UV range).

In this section, we revisit the approximative expressions for the ellipsometric quantities based on a linearization of the transfer matrix method in the film thickness d, as has been shown previously e.g. in [34, 35]. For the case of a thin film response in the infrared range, such an analytical approach is useful for the identification of the spectral features and the interpretation of the data in terms of the contrast between the responses of the film/substrate sample and the bare substrate. However, all models can be still calculated and fitted to the data in the full, correct, non-approximated form. If the response function of the substrate and the film thickness are known, one can also use a "brute force approach" by trying to evaluate the film/substrate response using a point-by-point fit procedure [36]. The approximative expressions are then helpful for understanding the sensitivity and its extrema.

Figure 1a illustrates the thin film geometry. The wavevector of the light that is incident from a vacuum ambient

under an angle of ϕ is given by $\bar{k} = (\xi, 0, q)\omega/c$, where $\xi = \sin\phi$ and $q = \cos\phi$ are the in-plane and normal geometrical components of the wavevector, respectively. The in-plane component, ξ, is an invariant and conserved across the parallel interfaces. The problem thus can be solved using only the normal components, thereby avoiding the evaluation of the complex angles of refraction. This convention is also better suited for a generalization for anisotropic systems [37, 38]. In the following, we denote the geometrical normal components of the wavevector in the film as κ and in the substrate as κ_s. Here we restrict ourselves to isotropic films with a dielectric response ε on isotropic substrates, with ε_s, in a vacuum ambient, $\varepsilon_{amb} = 1$. Such systems do not create a mixing between the p- and s-components of the light and thus can be described with a diagonal Jones matrix. This simplifies the transfer matrix method which can be solved separately for the s- and p-components in a 2×2 form. Within the Fresnel's convention, where the p-polarized reflection coefficient is defined as the ratio of x-components of the reflected and incident fields, $r_p = E_{rx}/E_{ix}$, the Fresnel's coefficients for the first ambient/film interface are written as:

$$r_{s1} = \frac{q - \kappa}{q + \kappa} \quad r_{p1} = \frac{\kappa - \varepsilon q}{\kappa + \varepsilon q}, \tag{1}$$

where $\kappa = \sqrt{\varepsilon - \xi^2}$. In analogy, the coefficients for the second interface can be expressed as:

$$r_{s2} = \frac{\kappa - \kappa_s}{\kappa + \kappa_s} \quad r_{p2} = \frac{\varepsilon\kappa_s - \varepsilon_s\kappa}{\varepsilon\kappa_s + \varepsilon_s\kappa}, \tag{2}$$

with $\kappa_s = \sqrt{\varepsilon_s - \xi^2}$. The coupling of the amplitudes of the electric fields across the stack is written, separately for s- and p-components, as

$$\begin{bmatrix} E_i \\ E_r \end{bmatrix} = \hat{M} \cdot \begin{bmatrix} E_t \\ 0 \end{bmatrix} = \hat{R}_1 \cdot \hat{\Phi} \cdot \hat{R}_2 \cdot \begin{bmatrix} E_t \\ 0 \end{bmatrix}, \tag{3}$$

where E_i, E_r, and E_t represent the in-plane components of the incident, reflected and transmitted fields, respectively. Here the x-component (y-component) accounts for the p-polarized (s-polarized) light and $\hat{R}_j$ is the interface matrix:

$$\hat{R}_j = \frac{1}{t_j}\begin{bmatrix} 1 & r_j \\ r_j & 1 \end{bmatrix}, \tag{4}$$

with the single interface transmission coefficients $t_{sj} = 1 + r_{sj}$ and $t_{pj} = 1 + r_{pj}$. Here t_p differs from the Fresnel's *amplitude* transmission coefficient as it is defined again in terms of in-plane components of the incident and transmitted fields: $t_p = E_{tx}/E_{ix}$. The propagation in the film is described by the

matrix $\hat{\Phi}$, which is identical for s- and p-components in an isotropic film, and will be approximated for $kd \ll 2\pi$ in a first order Taylor expansion:

$$\hat{\Phi} = \begin{bmatrix} e^{-ikd} & 0 \\ 0 & e^{ikd} \end{bmatrix} \rightarrow \hat{1} + ikd \begin{bmatrix} -1 & 0 \\ 0 & 1 \end{bmatrix}, \quad (5)$$

where, for the sake of brevity, the z-component of the physical wavevector, $\bar{k}$, is written as $k = \kappa\omega/c$. Within the linear approximation in the film thickness, d, the complete transfer matrix becomes

$$\hat{M} = \hat{R}_0 + ikd\hat{R}_1 \begin{bmatrix} -1 & 0 \\ 0 & 1 \end{bmatrix} \hat{R}_2, \quad (6)$$

where $\hat{R}_0$ is the interface matrix between the ambient and the bare substrate. From Eq. (3), the reflection coefficient of the whole stack is $r_{tot} = E_r/E_i = m_{21}/m_{11}$ and the relevant elements m_{11} and m_{21} are written as:

$$m_{11} = \frac{1}{t_0} + ikd\frac{r_1 r_2 - 1}{t_1 t_2}, \quad m_{21} = \frac{r_0}{t_0} + ikd\frac{r_2 - r_1}{t_1 t_2}, \quad (7)$$

where the r_0 and t_0 denote the coefficients for the ambient-bare substrate interface. Up to now, the expressions are identical for s- and p-polarized components. The reflection coefficients of the whole stack, r_{stot} and r_{ptot} are expressed as m_{s21}/m_{s11} and m_{p21}/m_{p11}, keeping them linear in d, and eventually the $\rho = r_{ptot}/r_{stot} = \tan\Psi.e^{i\Delta}$, up to linear terms:

$$\rho = \rho_0 \left(1 + i2dq\frac{\omega}{c} \cdot \frac{\varepsilon_s}{\varepsilon_s - 1} \cdot \frac{\varepsilon - 1}{\varepsilon} \cdot \frac{\varepsilon - \varepsilon_s}{1 - \varepsilon_s \cot^2 \phi} \right), \quad (8)$$

where once more, the ρ_0 is the ellipsometric response of the bare substrate. The resulting approximation (Eq. (8)) captures the essential effects, as it is proportional to thickness d, and to the contrast between the film and substrate, $\varepsilon - \varepsilon_s$. The factor $(\varepsilon - 1)/\varepsilon$ tends to unity for large values of ε (in the limit of a strong film response). For a vanishing film response of $\varepsilon = 1 (= \varepsilon_{amb})$ it approaches zero and for $\varepsilon \rightarrow 0$ it has a singularity which is known as the Berreman mode. Similarly, the factor $\varepsilon_s/(\varepsilon_s - 1)$ is close to unity for the case of a large substrate response, it leads to a singularity for $\varepsilon_s \rightarrow 1$ as the substrate reflection vanishes, and to zero contrast at $\varepsilon_s = 0$. The last factor in the denominator $(1 - \varepsilon_s \cot^2 \phi)$ represents the Brewster condition. For $\varepsilon_s \cot^2 \phi \rightarrow 1$ it leads to the improvement of the sensitivity near the Brewster angle of the substrate: the contrast between the bare substrate and film/substrate data in terms of the ellipsometric angles Ψ and particularly Δ will be large. On the other hand, the Brewster factor has a detrimental effect for large ε_s, that is, far from the Brewster condition.

The pre-factor $d\omega/c$ can be interpreted in terms of the diminishing sensitivity to a film with given thickness for long wavelengths, or the factor $i\omega$ can be seen as multiplying the $(\varepsilon - \varepsilon_s)$ contrast, leading to a contrast in
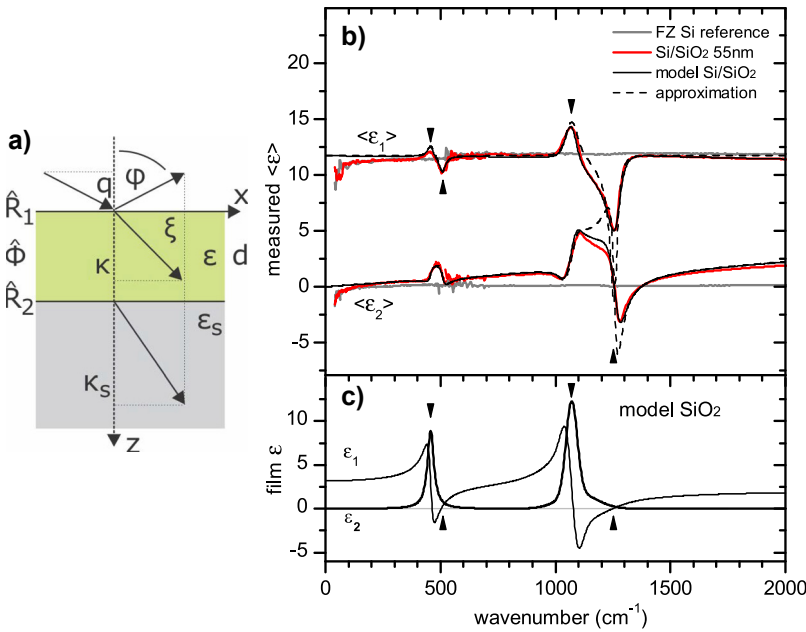

Figure 1: (a) Schematic of the ambient/film/substrate system with the geometrical components of the wave vectors. (b) Infrared ellipsometric spectra of bare silicon (grey lines) and silicon with 55 nm of thermal SiO₂ (red lines), measured at $\phi = 75°$. Exact model (black solid line) and the approximation of Eq. (9) (dashed line). (c) Dielectric function of SiO₂ used for the model calculations. Black arrows point to the TO and LO phonon features in the spectra.

optical conductivity ($\sigma = -i\omega.\epsilon_0.(\epsilon-1)$), up to the vacuum permittivity constant ϵ_0.

With a few more steps, one arrives at the following approximate formula for the measured pseudo-dielectric function:

$$\langle\varepsilon\rangle = \varepsilon_s + 2d\kappa_s\frac{\varepsilon_s}{\varepsilon_s-1}\cdot\frac{\varepsilon-1}{\varepsilon}\cdot\frac{-i\omega}{c}\,(\varepsilon-\varepsilon_s), \qquad (9)$$

where the familiar contrast factors $(\varepsilon-1)/\varepsilon$ and $\varepsilon_s/(\varepsilon_s-1)$ reappear, while the Brewster factor $(1-\varepsilon_s\cot^2\phi)$, i.e. the enhancement of the contrast near the Brewster condition has disappeared: the contrast between the bare substrate and film/substrate data in terms of the pseudo-dielectric function will not show extreme at the Brewster condition as seen in terms of Ψ and Δ. Nevertheless, the relative sensitivity near the Brewster condition is still improved since the deduced $\langle\varepsilon_s\rangle$ and $\langle\varepsilon\rangle$ numerical values will have the least error propagated from the experimental Ψ and Δ error bars. We have grouped together the factors $-i\omega(\varepsilon-\varepsilon_s)$ to highlight the connection between the contrast of the measured pseudo-dielectric function $\langle\varepsilon\rangle$ of an ultrathin film and the corresponding contrast in the optical conductivity. It has the slightly counterintuitive property that in the parts of the spectrum where the substrate is transparent, the features of film's σ_1 show up in the $\langle\varepsilon_1\rangle$ spectra and the features of σ_2 appear in $\langle\varepsilon_2\rangle$ [26]. This behavior changes in the reststrahlen bands of the substrate, where the pre-factor κ_s becomes imaginary, such that for the film response the features of σ_1 appear in $\langle\varepsilon_2\rangle$ and features of $-\sigma_2$ in $\langle\varepsilon_1\rangle$.

At first, we illustrate the above-described effects for the example of a 55 nm thick film of thermal SiO$_2$ on undoped silicon. Figure 1b shows the infrared pseudo-dielectric function as measured on a bare Silicon substrate and the one with the SiO$_2$ film on top. The solid line represents the correct transfer matrix model, while the dashed line is an approximation calculated from Eq. (9). The model dielectric function of SiO$_2$ that was used for both calculations is plotted in Figure 1c. The two TO phonon peaks of SiO$_2$ at 458 and 1070 cm^{-1}, marked with downward arrows in Figure 1b and c, appear as peaks in $\langle\varepsilon_1\rangle$ and "S"-shaped, σ_2-like features appear in $\langle\varepsilon_2\rangle$. At the LO frequencies of the film response at 510 and 1254 cm^{-1}, that are marked with upward arrows, the Berreman modes show up in terms of dips in $\langle\varepsilon_1\rangle$ and corresponding "Z"-shaped features in $\langle\varepsilon_2\rangle$. For the low frequency mode which has a relatively small TO-LO splitting the above-described features are partially overlapping and therefore less obvious. For the high frequency phonon, however, the TO-LO splitting is larger, and these features are well separated and thus can be clearly seen. The overall slope in $\langle\varepsilon_2\rangle$ is caused by the sloping $\sigma_2(\omega)\approx\omega(\varepsilon_\infty-1)$, where

ε_∞ is the high frequency dielectric constant. In this example, the approximative formula for $\langle\varepsilon\rangle$ (dashed lines) agrees with the exact model (solid lines), apart from the overestimated strength of the Berreman mode at 1254 cm^{-1}.

We note that the clear identification of the TO and LO features of the ultrathin film can, in some favorable cases, be used for determining both the optical response and the thickness of the ultrathin film. The overall contrast is proportional to $d.\Delta\sigma$. For an isotropic film, with a clear phonon spectrum, the magnitude of the TO-LO splitting is a measure of the oscillator strength of the phonon mode; the film thickness can thus be deduced from the overall value of the contrast. In reality, this approach is not very practical due to additional correlations with the phonon broadenings, and possible tetragonality of the strained film, as will be discussed below. Nevertheless, a similar approach has been utilized to determine the thickness, density and mobility of a 2D electron gas at an oxide heterointerface [39].

The 2×2 transfer matrix formalism can be generalized also for the case of an orthorhombic substrate and thin film, as long as the high symmetry axes remain parallel to the xyz coordinate system of the instrument. The approximative expressions, however, loose some of the clarity and simplicity of the expression in Eqs. (8) and (9). In this respect, we will only discuss two intermediate cases: a tetragonal film on an isotropic substrate, and an isotropic film on a tetragonal substrate, for both of which the high symmetry tetragonal c axis is parallel to z. These configurations are relevant for the materials discussed here, for which the strained film on an isotropic substrate is expected to become tetragonal, and one of the substrates, SrLaGaO$_4$, has a tetragonal crystal structure.

For a tetragonal film with the in-plane response $\varepsilon_\parallel$ and out-of-plane response $\varepsilon_\perp$, Eq. (8) acquires the following form:

$$\frac{\rho}{\rho_0} = 1 + i2dq\frac{\omega}{c}\cdot\frac{\varepsilon_s}{\varepsilon_s-1}\cdot\frac{1}{f_B}\cdot\left[(\varepsilon_\parallel-\varepsilon_s)+\left(\frac{\varepsilon_s}{\varepsilon_\perp}-1\right)\right], \quad (10)$$

where the symbol f_B denotes the Brewster factor, $f_B = 1-\varepsilon_s\cot^2\phi$, and the film response contributes by two terms, with one being the contrast of the in-plane response to the substrate $(\varepsilon_\parallel-\varepsilon_s)$, while the out-of-plane component, $\varepsilon_\perp$, is responsible for the Berreman modes, with the term $(\varepsilon_s/\varepsilon_\perp-1)$. As compared to Eq. (8), the pre-factor $(\varepsilon-1)/\varepsilon$ is now contained in the square bracket. The pseudo-dielectric function can be expressed in analogy to Eq. (9).

In the case of an isotropic film on a tetragonal substrate, we denote the in-plane response of the substrate as ε_{ab}, and the out-of-plane as ε_c, while the isotropic film is described by ε,

$$\frac{\rho}{\rho_0} = 1 + i2dq \frac{\omega}{c} \cdot \frac{\varepsilon_{ab}}{\varepsilon_{ab} - 1} \cdot \frac{\varepsilon - 1}{\varepsilon} \cdot \frac{1}{f_B} \cdot (\varepsilon - \varepsilon_s'). \quad (11)$$

The general structure remains analogous to Eq. (8), with a generalized Brewster factor, f_B, and an effective substrate response ε_s':

$$f_B = 1 - \varepsilon_s' \cot^2 \phi, \quad \varepsilon_s' = \varepsilon_c \frac{\varepsilon_{ab} - 1}{\varepsilon_c - 1}. \quad (12)$$

In this case the derivation of the pseudo-dielectric response of the film is not very elegant since it requires an expression for the pseudo-dielectric response of the tetragonal substrate itself.

4 Results and discussion

A SrMnO₃ thin film grown on a LaAlO₃ (001) substrate is subject to a small compressive strain of about −0.3%. The LaAlO₃ substrate has a slightly rhombohedral structure, but due to its natural twinning, the ellipsometric spectra resemble the ones of an isotropic material with some additional phonon modes [40]. The infrared spectrum of LaAlO₃ exhibits three strong and sharp phonon lines at 182, 426, and 652 cm⁻¹, and two weak ones at 496 and 692 cm⁻¹. Figure 2a shows the room temperature ellipsometric data in terms of Ψ, Δ of the bare LaAlO₃ substrate and the sample with a 30 nm film of SrMnO₃, measured in the infrared and THz range at $\phi = 75°$. For clarity, we show only the model dielectric function of LaAlO₃ in Figure 2b, together with the calculated pseudo-dielectric function of the film/substrate sample. Figure 2c shows the contrast due to the film in terms of the difference spectra of Ψ and Δ, between the sample and the LaAlO₃ substrate. Also shown for comparison are the difference spectra of a correctly calculated model, i.e. without the approximation that were discussed in the previous section. The film dielectric response, obtained from fitting the differential data is plotted in Figure 2d.
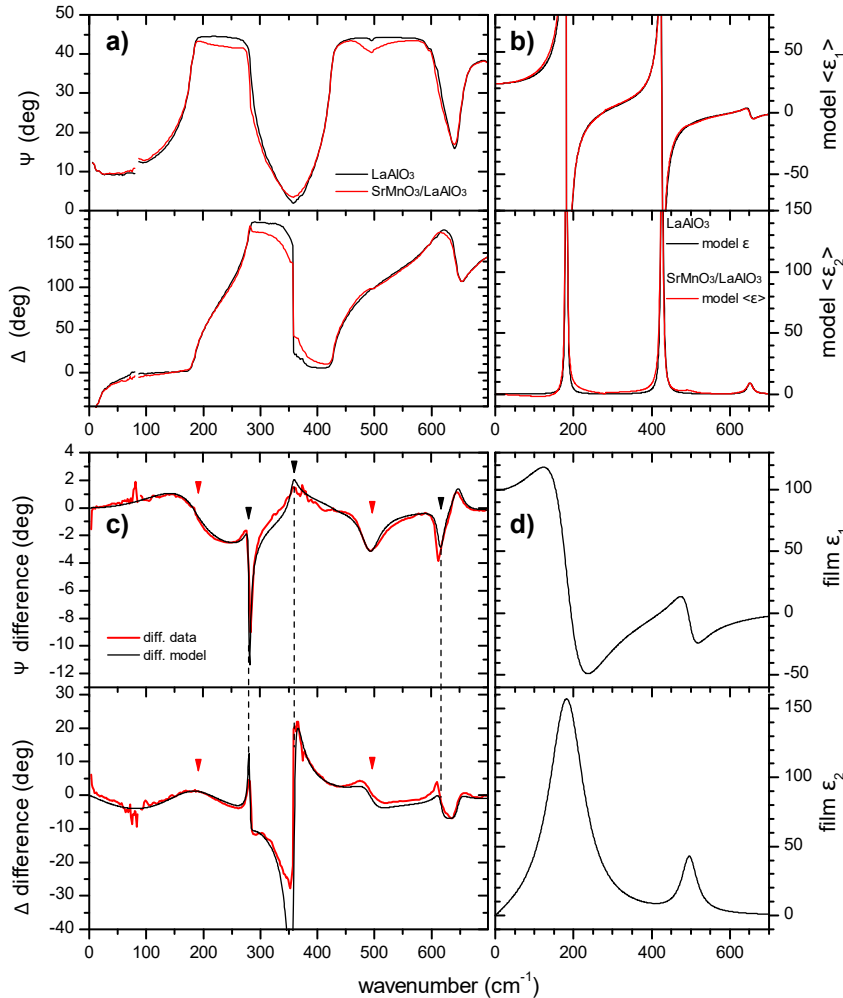

Figure 2: Ellipsometric spectra at 300 K of a SrMnO₃ (30 nm) film on a LaAlO₃ substrate. (a) Ellipsometric angles Ψ, Δ measured for a bare LaAlO₃ substrate (black), and the SrMnO₃ film on LaAlO₃ (red) at $\phi = 75°$. (b) Model dielectric function of LaAlO₃ (black) and model pseudo-dielectric function, $\langle\varepsilon\rangle$, of the SrMnO₃ film on LaAlO₃ (red). (c) Difference between the Ψ and Δ datasets (red) and the corresponding differential model (black). Red arrows mark the position of the TO phonons of the film. Black arrows and the vertical dashed lines mark the sensitivity extrema due to the properties of the LaAlO₃ substrate. (d) Deduced model dielectric function of SrMnO₃.

The modeling of thin film data in the infrared range is complicated by imperfections of both the data and the model. Since the changes of the spectra due to the film response are small, even a slight discrepancy between the measured data and the model of the bare substrate can lead to substantial errors in the modeling of the thin film response. The analysis of the differential spectra therefore represents a pragmatic approach to alleviate this problem. The Ψ and Δ data in the Figure 2a show several systematic trends: (i) The THz part of the spectrum suffers from diffraction artefacts [41]. (ii) The low frequency part of the continuous-wave infrared spectrum is affected by the incoherent back-side reflection that is visible as an up-turn of Ψ below 100 cm^{-1}. (iii) The rotating analyzer data are rather poor as Ψ approaches zero in the range around 350 cm^{-1}. (iv) Nonideality of the polarizers [42] affects the spectra, particularly towards higher frequencies. While some of the imperfections can be treated by improved experimental design or calibration procedures – as will be discussed elsewhere – they cannot be completely avoided. Nevertheless, these artificial features tend to cancel out in the difference plots between the response of the sample

and the bare substrate. At the same time, an accurate model of the substrate response might require asymmetric phonon line shapes due to a mode coupling, a Gaussian broadening due to disorder, and other subtle effects. Here, we have not considered such additional complications and described the response of the phonon of the LaAlO₃ substrate with three harmonic oscillators (see Figure 2b) and the response of the SrMnO₃ film with two harmonic oscillators (Figure 2d). The comparison of the difference plots for the measured (red) and model (black) data in Figure 2c shows a rather good agreement that justifies this approach. The approximative expression of Eq. (8) can be used to identify the strong features in the contrast that are caused by the film or substrate properties.

We can reliably identify two features that originate from the film. Their positions, marked by the red arrows in Figure 2c, agree well with the TO1 and TO3 modes of bulk SrMnO₃ [11]. Note that TO1 (Slater) mode of the film at 191 cm^{-1} is rather strong and broad, similar as reported for bulk SMO, and thus governs the overall shape of the contrast in Ψ and Δ below 250 cm^{-1}. We assume that the TO2 mode of the film is too weak and broad to be identified. The position of the TO3
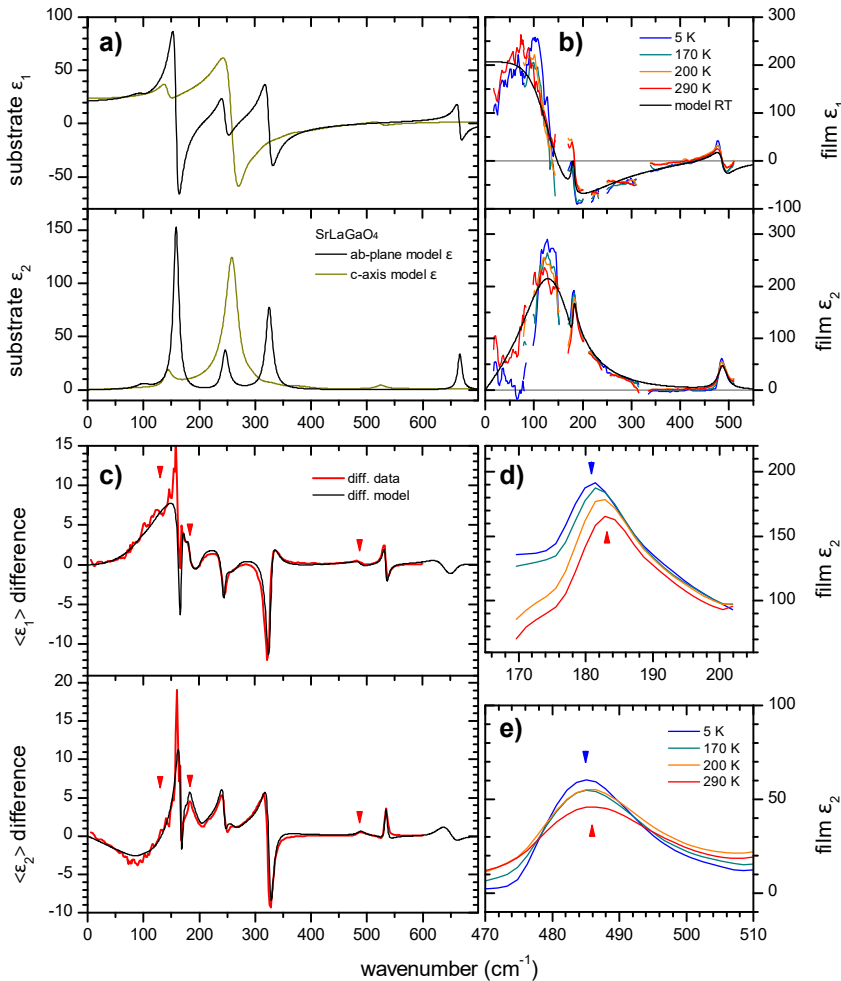

Figure 3: Ellipsometry spectra of SrMnO₃ (30 nm) on SrLaGaO₄. (a) Model calculations of the anisotropic dielectric response of a tetragonal SrLaGaO₄ substrate at room temperature. Shown are the ab-plane (001) response (black) and the c-axis [001] response (dark yellow). (b) Temperature dependence of the SrMnO₃ dielectric response calculated point-by-point from the differential <ε> data (coloured lines), and from a three-phonon model at room temperature (black line). (c) Difference between the ellipsometric <ε> spectra of the film/substrate sample and the bare substrate, measured at room temperature and $\phi = 75°$ (red). Corresponding differential spectra for a model that includes the anisotropy of the substrate and assumes an isotropic film (black) with three TO phonons that are marked by red arrows. (d) Detailed temperature dependence near the TO2 phonon of SrMnO₃. (e) Detailed temperature dependence near the TO3 phonon of SrMnO₃. The arrows mark the position of the phonons at 290 K (red) and 5 K (blue).

(Axe) mode at 497 cm^{-1} again corresponds well to the reported bulk response. In Figure 2c, we have also marked with black arrows and vertical dashed lines some sharp features that are due to the substrate response. The features around 280 and 620 cm^{-1} mark the frequencies at which $\varepsilon_s \to 1$. At the pronounced maximum around 350 cm^{-1} the substrate dielectric function fulfils the Brewster condition for the angle of incidence of 75°. Finally, the contrast around 650 cm^{-1} is due to the substrate TO phonon at 652 cm^{-1}.

Figure 3 shows the ellipsometric data and the modelling of the dielectric response of the SrMnO₃ (30 nm) film that was deposited on a tetragonal SrLaGaO₄ (001) substrate which yields an in-plane epitaxial strain of +1.1%. The response of the SrLaGaO₄ substrate in Figure 3a reveals a strong anisotropy with respect to the in-plane (ab) and normal (c) components and some rather asymmetric phonon line-shapes [43, 44]. It has been obtained by fitting the ellipsometric spectra of SrLaGaO₄ (001) and (100) substrates at room temperature with the approximative model of ref. [44], while allowing for a coupling of the phonon modes. The temperature dependent response has been measured for both the ab-plane dominated response on the (001) cut crystal and the c-axis response on the (100) cut crystal. The corresponding response of the SrMnO₃ on SrLaGaO₄ (001) sample was also measured at temperatures between 5 and 300 K. The room temperature difference spectrum between the pseudo-dielectric functions of the thin film sample and the bare substrate is shown in Figure 3c by the red lines. The corresponding difference spectrum for a model that accounts for the tetragonal substrate and an isotropic film with three phonon modes is shown by the black line. The positions of the SrMnO₃ phonons at 130, 183, 487 cm^{-1} are marked by red arrows in Figure 3c. The three strong TO modes of the ab-response of the SrLaGaO₄ substrate give rise to the rather sharp features around 167, 245, 326 cm^{-1} and the feature at 534 cm^{-1} marks the frequency at which for the substrate $\varepsilon_{ab} \to 1$.

Although the parameterized model of the SrMnO₃ dielectric function reproduces the experimental data qualitatively, further insight can be gained from a point-by-point fit. For the substrate, we used a temperature dependent anisotropic model. The parameterized dielectric model of the isotropic film was used as a starting point at each frequency to fit the unconstrained ε_1 and ε_2 values of the film. The calculated difference has been fitted to the differential $\langle\varepsilon\rangle$ data. The obtained response functions are plotted in Figure 3b at selected temperatures. We have removed here the parts of the spectra at which the strong TO features of the substrate give rise to large discrepancies. The three SrMnO₃ phonons are still clearly discernible. The broad TO1 mode, with a maximum around 130 cm^{-1} is significantly softer than

in bulk SMO or in the SMO film on the LaAlO₃ substrate. The temperature dependence was performed with 30 K steps, and we observed a substantial change of the SrMnO₃ TO1 mode between 170 and 200 K. Upon cooling, the mode width is reduced, and its position is shifted to higher frequency. A corresponding behavior was observed at the antiferromagnetic phase transition in bulk SrMnO₃ and Sr$_{1-x}$Ba$_x$MnO₃ crystals [11] and ceramics [12], where it was attributed to a strong spin-phonon coupling. The TO2 and TO3 modes exhibit a corresponding softening upon cooling. The temperature dependence of the ε_2 spectra of the TO2 mode is detailed in Figure 3d, where the arrows mark the phonon position at 290 K (red arrow at 183 cm^{-1}) and at 5 K (blue arrow at 181 cm^{-1}). Figure 3e details the temperature dependence of the TO3 phonon, which acquires an asymmetric line-shape at low temperatures and softens slightly from 486 cm^{-1} at 295 K (red arrow) to 485 cm^{-1} at 5 K (blue arrow).

Figure 4 shows the ellipsometry data and their analysis for a 30 nm thick SrMnO₃ film on an LSAT (La$_{0.3}$Sr$_{0.7}$) (Al$_{0.65}$Ta$_{0.35}$)O₃ substrate. The latter yields a tensile strain of 1.7 %. It has a cubic perovskite structure with an isotropic infrared response but due to its complex composition it exhibits a large number of infrared-active phonon modes [45]. The ellipsometry data on a bare LSAT substrate and on the SrMnO₃/LSAT sample are plotted in Figure 4a in terms of a pseudo-dielectric function. Apart from the 157 cm^{-1} mode, the remaining LSAT phonons are not particularly sharp or strong which makes it a suitable substrate for an analysis of the thin film response. However, by studying several LSAT substrates (from different growth batches) we found that their optical response is not fully reproducible. Particularly, for the range between 200 and 300 cm^{-1} their response varies from sample to sample by up to 10% in the value of ε_2. The substrate data shown in Figure 4a were therefore obtained on the very same LSAT specimen that was subsequently used as substrate for the SrMnO₃ growth.

Figure 4c shows the difference spectra of the pseudo-dielectric functions of the thin film sample with respect to the bare LSAT substrate. The differential model line in Figure 4c was again obtained in two steps. First, the LSAT phonon model was fitted to the bare substrate data, then the three-phonon SrMnO₃ model was obtained by fitting the differential data. We found that the fit quality could be further improved if some of the substrate parameters (phonon strengths) were allowed to vary during the fitting with the film model. The resulting substrate response showed only minor differences from the model fitted *a-priori*, but the matching between the difference model and the differential data was substantially improved. The obtained dielectric function of the SrMnO₃ film is displayed
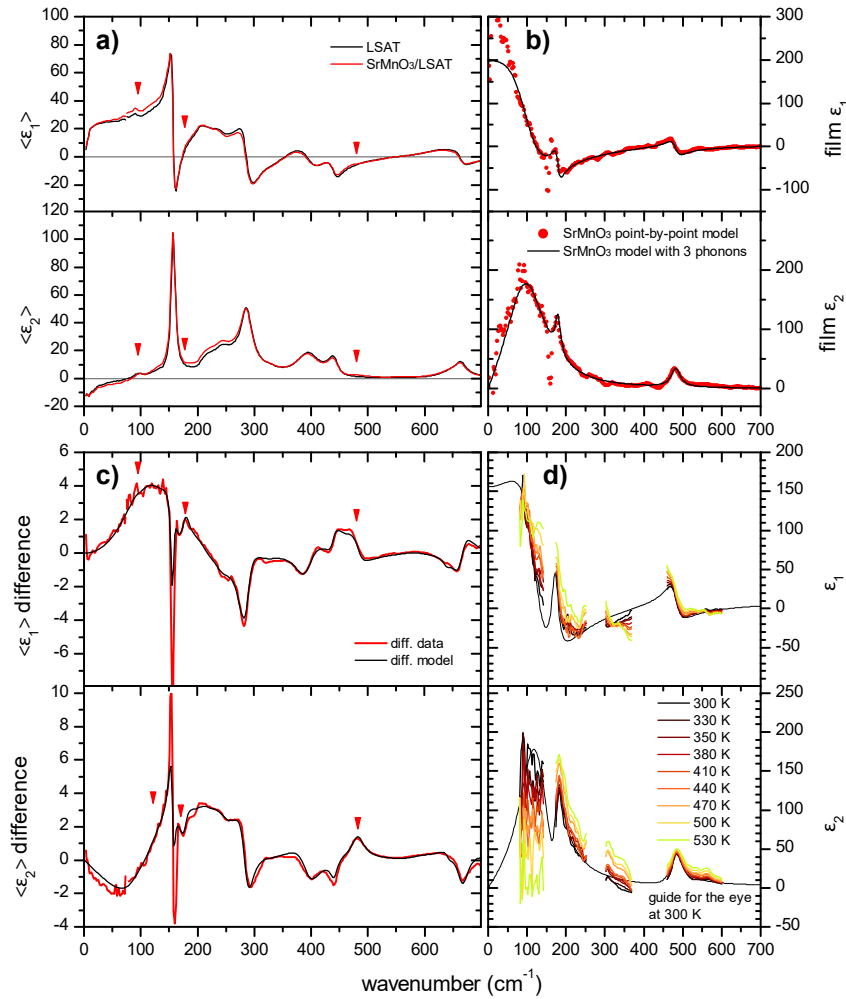
Figure 4: SrMnO₃ (30 nm) on LSAT. (a) Experimental pseudo-dielectric function <ε> of a bare LSAT substrate (black) and a SrMnO₃/LSAT sample (red), at room temperature and $\phi = 75°$. (b) Dielectric response of the SrMnO₃ film at room temperature parameterized with three phonons (black line) and extracted point-by-point (red symbols). (c) Difference between the ellipsometric <ε> spectra of the film/substrate sample and bare substrate (red), as plotted on panel (a), and the corresponding differential model (black) with three TO phonons of SrMnO₃ marked by the red arrows. (d) High-temperature evolution of the SrMnO₃ response (for a different sample).

in Figure 4b (black line). The point-by-point model (red symbols) was obtained by fitting the differential data, using the previously optimized substrate/film model as a starting point at each frequency, while varying only the unconstrained ε_1 and ε_2 values of the film.

The TO1, TO2, and TO3 modes of the SrMnO₃ film on the LSAT substrate exhibit a significant softening as compared to bulk SMO and the SMO films on the other substrates that are less strained. However, the low-temperature spectra of the SMO phonon modes revealed no sign of an anomaly due to a ferroelectric transition, at least not within the limited precision of our experiment. According to the previous report of Becher at al. [19], the polar order of SMO strained on LSAT sets in at temperatures well above 300 K. For this reason, we have also attempted to measure the optical response at elevated temperatures. Figure 4d shows the dielectric function of the SMO film at temperatures between 300 and 560 K, as obtained with the point-by-point analysis method. Note that this high temperature

experiment has been performed on a different sample than the one for which the data and analysis are presented in Figure 4a–c. Moreover, the elevated temperature dependence of the bare LSAT substrate has been performed on a different specimen than the one on which the SMO film was grown. Accordingly, the extracted dielectric response of the SMO film suffers from an imperfect substrate model and in these frequency ranges the data have been omitted from the plots. The obtained data in Figure 4d reveal a temperature dependent loss of the low-energy spectral weight that can be attributed to the TO1 mode around 100 cm⁻¹, which with increasing temperature seems to get shifted toward higher frequencies around 200–300 cm⁻¹. However, upon cooling the sample back to room temperature we found that these changes were persistent and thus at least partially related to some irreversible change of the properties of the thin film sample. The most likely cause is due to a partial loss of oxygen, as the heating experiment was done in high vacuum.
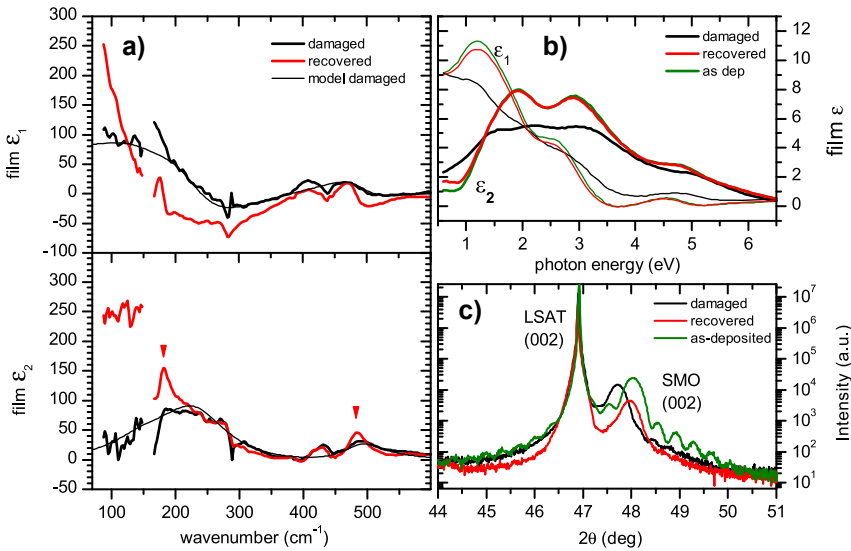
Figure 5: Room temperature properties of a SrMnO₃ film on LSAT, before and after oxygen annealing. (a) Infrared optical response of the SrMnO₃ film that was damaged after a high-temperature experiment (black line) and was recovered after by a O₂ annealing (red line), in terms of a point-by-point analysis of the dielectric function, and an approximation with a two-phonon model for the damaged sample (thin black line). Red arrows point to the recovered sharp TO2 and TO3 modes. (b) Near infrared to ultraviolet spectra of the SrMnO₃ film, in terms of a point-by-point fit of the dielectric function, of the as-deposited sample (green), damaged (black), and after O₂ annealing (red). (c) X-ray diffraction (CuKα) pattern in the vicinity of (002) BRAGG peaks, of the as-deposited (green), damaged (black), and O₂ post-annealed samples (red).

Accordingly, using a high-pressure high-temperature chamber, we have annealed the damaged SrMnO₃/LSAT sample in 5 bar of O₂ at 300 °C for 3 h. Near-infrared to UV ellipsometry spectra and X-ray diffraction 2θ scans were measured on this sample before and after the high pressure O₂ annealing. We have also prepared a freshly deposited SrMnO₃/LSAT sample for comparison. The obtained data document that it was possible to reoxygenate the SrMnO3

Figure 6: Summary of the strain dependence of the phonon parameters of SrMnO₃ films at room temperature. Bulk values are taken from reference [11].

film and recover its initial oxidation state. Figure 5a shows the infrared spectra of the SrMnO₃ film of the damaged sample (black line) and after the O₂ annealing (red line). A simple two phonon model (thin black line) of the response of the damaged sample serves as guide for the eye and shows the broad TO1 mode centred above 200 cm⁻¹, as well as broadening of the TO3 mode. After the O₂ annealing (red line), the TO1 mode restores its weight and position around 100 cm⁻¹, while the TO2 and TO3 modes sharpen, and the spectrum qualitatively resembles the results plotted in Figure 4b. Figure 5b shows the NIR-UV dielectric response of the film that is governed by inter-band transitions. While the response of the damaged sample shows a strong broadening, after the O₂ annealing, the peaks appear almost identical to the freshly deposited sample (green lines). Finally, Figure 5c compares the X-ray diffraction data of the (002) Bragg peaks of the LSAT substrate and the SrMnO₃ film for the as-deposited (green), damaged (black) and O₂ annealed (red) samples. The estimated c-axis lattice parameter of the as-deposited sample is 3.784 Å. In the damaged state it increases to 3.809 Å, consistent with an expansion of the unit cell volume due to the formation of oxygen vacancies. Eventually, the c-axis lattice parameter of the recovered sample is 3.788 Å, which is close to the value of the as-deposited state, although the absence of the thickness fringes indicates an enhanced surface roughness of the film in both the damaged and recovered states.
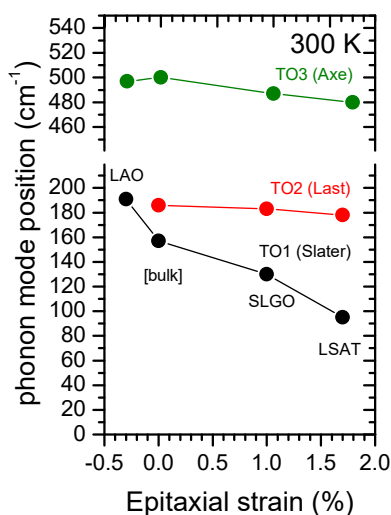
5 Conclusions

With infrared and terahertz ellipsometry we have studied how the infrared phonons of 30 nm thick SrMnO$_3$ films on LaAlO$_3$, SrLaGaO$_4$, and LSAT substrates are affected by the epitaxial strain. Apart from the sample grown on LaAlO$_3$, we observed the three expected infrared-active phonon modes of SrMnO$_3$ and their softening with increasing strain that is summarized in Figure 6. For the SMO film grown on the SrLaGaO$_4$ substrate, the TO1 Slater mode was found to exhibit an anomalous temperature dependence (sudden narrowing and blue shift) in the vicinity of the expected AF transition around 170 K that is indicative of a strong spin-phonon coupling. The strong TO1 phonon mode of SrMnO$_3$ is also most sensitive to the in-plane strain (soft-mode) and our data suggest that a higher tensile strain is needed to induce a ferroelectric transition at room temperature. The observed behavior is consistent with the cited theoretical and experimental literature on (Ca,Sr,Ba)MnO$_3$ systems and related films. For the SMO film on LSAT, we have shown that the optical response is very sensitive to the loss of oxygen and the possibility to recover this loss by reoxygenating the film with a high-pressure oxygen annealing procedure.

We have also presented the approximative expressions for the ellipsometric response of a film/substrate system in the ultrathin film limit ($d << \lambda$) that are useful for understanding the sensitivity of the experimental data to the response of the thin film. In particular, the experiment is sensitive to the in-plane optical conductivity of the film, $\varepsilon_\parallel$, while the normal component of the dielectric tensor $\varepsilon_\perp$ contributes as $\approx \omega/\varepsilon_\perp$. The latter gives rise to Berreman modes that are not resolved in our far-infrared data. Sensitivity extrema originating from the substrate properties have also been identified.

The three used substrates, while they are similar oxides, display different infrared optical properties: LaAlO$_3$ has strong and sharp modes, SrLaGaO$_4$ is tetragonal with coupled phonons and LSAT has many broad modes showing a sizeable variance among different specimens. To tackle these issues, we have developed methods for the analysis of difference spectra and presented strategies for extracting the optical response of the thin films.

References

[1] M. Schubert, *Infrared Ellipsometry on Semiconductor Layer Structures*, Heidelberg, Springer, 2004.

[2] M. Neshat and N. P. Armitage, "Developments in THz range ellipsometry," *J. Infrared, Millim. Terahertz Waves*, vol. 34, p. 682, 2013.

[3] D. N. Basov and T. Timusk, "Electrodynamics of high-T$_c$ superconductors," *Rev. Mod. Phys.*, vol. 77, p. 721, 2005.

[4] D. N. Basov, R. D. Averitt, D. van der Marel, M. Dressel, and K. Haule, "Electrodynamics of correlated electron materials," *Rev. Mod. Phys.*, vol. 83, p. 471, 2011.

[5] Y. Tokura, "Critical features of colossal magnetoresistive manganites," *Rep. Prog. Phys.*, vol. 69, p. 797, 2006.

[6] J. H. Lee, L. Fang, E. Vlahos, et al., "A strong ferroelectric ferromagnet created by means of spin–lattice coupling," *Nature*, vol. 466, p. 954, 2010.

[7] J. Chakhalian, A. J. Millis, and J. Rondinelli, "Whither the oxide interface," *Nat. Mater.*, vol. 11, pp. 92–94, 2012.

[8] J. M. Rondinelli and N. A. Spaldin, "Structure and properties of functional oxide thin films: insights from electronic-structure calculations," *Adv. Mater.*, vol. 23, p. 3363, 2011.

[9] O. Chmaissem, B. Dabrowski, S. Kolesnik, et al., "Relationship between structural parameters and the Néel temperature in Sr$_{1-x}$Ca$_x$MnO$_3$ (0≤x≤1) and Sr$_{1-y}$Ba$_y$MnO$_3$ (y≤0.2)," *Phys. Rev. B*, vol. 64, 2001, Art. no. 134412.

[10] H. Sakai, J. Fujioka, T. Fukuda. et al., "Displacement-type ferroelectricity with off-center magnetic ions in perovskite Sr$_{1-x}$Ba$_x$MnO$_3$," *Phys. Rev. Lett.*, vol. 107, 2011, Art. no. 137601.

[11] H. Sakai, J. Fujioka, T. Fukuda, et al., "Soft phonon mode coupled with antiferromagnetic order in incipient-ferroelectric Mott insulators Sr$_{1-x}$Ba$_x$MnO$_3$," *Phys. Rev. B*, vol. 86, 2012, Art. no. 104407.

[12] S. Kamba, V. Goian, V. Skoromets, et al., "Strong spin-phonon coupling in infrared and Raman spectra of SrMnO$_3$," *Phys. Rev. B*, vol. 89, 2014, Art. no. 064308.

[13] S. Bhattacharjee, E. Bousquet, and P. Ghosez, "Engineering multiferroism in CaMnO$_3$," *Phys. Rev. Lett.*, vol. 102, 2009, Art. no. 117602.

[14] J. H. Lee and K. M. Rabe, "Epitaxial-Strain-Induced Multiferroicity in SrMnO$_3$ from First Principles," *Phys. Rev. Lett.*, vol. 104, 2010, Art. no. 207204.

[15] J. Hong, A. Stroppa, J. Iniguez, S. Picozzi, and D. Vanderbilt, "Spin-phonon coupling effects in transition-metal perovskites: A DFT + U and hybrid-functional study," *Phys. Rev. B*, vol. 85, 2012, Art. no. 054417.

[16] V. Goian, S. Kamba, F. Borodavka, D. Nuzhnyy, M. Savinov, and A. A. Belik, "The manifestation of spin-phonon coupling in CaMnO$_3$," *J. Appl. Phys.*, vol. 117, 2015, Art. no. 164103.

[17] A. Edström and C. Ederer, "First-principles-based strain and temperature-dependent ferroic phase diagram of $SrMnO_3$," *Phys. Rev. Mater.*, vol. 2, 2018, Art. no. 104409.

[18] T. Günter, E. Bousquet, A. David, et al., "Incipient ferroelectricity in 2.3% tensile-strained $CaMnO_3$ films," *Phys. Rev. B*, vol. 85, 2012, Art. no. 214120.

[19] C. Becher, L. Maurel, U. Aschauer, et al., "Strain-induced coupling of electrical polarization and structural defects in $SrMnO_3$ films," *Nat. Nanotechnol.*, vol. 10, pp. 661–666, 2015.

[20] J. W. Guo, P.S. Wang, Y. Yuan, et al., "Strain-induced ferroelectricity and spin-lattice coupling in $SrMnO_3$ thin films," *Phys. Rev. B*, vol. 97, 2018, Art. no. 235135.

[21] F. Wang, Y. Q. Zhang, Y. Bai, et al., "Oxygen vacancy formation, crystal structures, and magnetic properties of three $SrMnO_{3-\delta}$ films," *Appl. Phys. Lett.*, vol. 109, 2016, Art. no. 052403.

[22] P. Agrawal, J. Guo, P. Yu, et al., "Strain-driven oxygen deficiency in multiferroic $SrMnO_3$ thin films," *Phys. Rev. B*, vol. 94, 2016, Art. no. 104101.

[23] L. Maurel, N. Marcano, E. Langenberg, et al., "Engineering the magnetic order in epitaxially strained $Sr_{1-x}Ba_xMnO_3$ perovskite thin films," *Apl. Mater.*, vol. 7, 2019, Art. no. 041117.

[24] V. Goian, E. Langenberg, N. Marcano et al., "Spin-phonon coupling in epitaxial $Sr_{0.6}Ba_{0.4}MnO_3$ thin films," *Phys. Rev. B*, vol. 95, 2017, Art. no. 075126.

[25] J. Petzelt and S. Kamba, "Far infrared and terahertz spectroscopy of ferroelectric soft modes in thin films: A review," *Ferroelectrics*, vol. 503, pp. 19–44, 2016.

[26] P. Marsik, K. Sen, J. Khmaladze, M. Yazdi-Rizi, B. P. P. Mallett, and C. Bernhard, "Terahertz ellipsometry study of the soft mode behavior in ultrathin $SrTiO_3$ films," *Appl. Phys. Lett.*, vol. 108, 2016, Art. no. 052901.

[27] K. Sen, P. Marsik, S. Das, et al., "Superconductivity and charge-carrier localization in ultrathin $La_{1.85}Sr_{0.15}CuO_4/La_2CuO_4$ bilayers," *Phys. Rev. B*, vol. 95, 2017, Art. no. 214506.

[28] B. P. P. Mallett, J. Khmaladze, P. Marsik, et al., "Granular superconductivity and magnetic-field-driven recovery of macroscopic coherence in a cuprate/manganite multilayer," *Phys. Rev. B*, vol. 94, no. R, 2016, Art. no. 180503.

[29] C. Bernhard, J. Humlicek, and B. Keimer, "Far-infrared ellipsometry using a synchrotron light source - the dielectric response of the cuprate high T_c superconductors," *Thin Solid Films*, vol. 455–456, pp. 143–149, 2004.

[30] C. M. Morris, R. Valdes Aguilar, A. V. Stier, and N. P. Armitage, "Polarization modulation time-domain terahertz polarimetry," *Opt. Express*, vol. 20, no. 11, 2012, Art. no. 12303.

[31] M. Neshat and N. P. Armitage, "Terahertz time-domain spectroscopic ellipsometry: instrumentation and calibration," *Opt. Express*, vol. 20, no. 27, 2012, Art. no. 29063.

[32] L. Maurel, N. Marcano, T. Prokscha, et al., "Nature of antiferromagnetic order in epitaxially strained multiferroic $SrMnO_3$ thin films," *Phys. Rev. B*, vol. 92, 2015, Art. no. 024419.

[33] J. Humlicek, "Polarized light and ellipsometry," in *Handbook of Ellipsometry*, H. Tompkins and E. Irene, Eds., New York, William Andrew Publishing, 2005, pp. 80–90.

[34] D. W. Berreman, "Infrared absorption at longitudinal optic frequency in cubic crystal films," *Phys. Rev.*, vol. 130, p. 2193, 1963.

[35] D. E. Aspnes, "Optical properties of thin films," *Thin Solid Films*, vol. 89, pp. 249–262, 1982.

[36] P. Fris, D. Munzar, O. Caha, and A. Dubroka, "Direct observation of double exchange in ferromagnetic $La_{0.7}Sr_{0.3}CoO_3$ by broadband ellipsometry," *Phys. Rev. B*, vol. 97, 2018, Art. no. 045137.

[37] D. W. Berreman, "Optics in stratified and anisotropic media: 4X4-Matrix formulation," *J. Opt. Soc. Am.*, vol. 62, p. 502, 1972.

[38] M. Schubert, "Polarization-dependent optical parameters of arbitrarily anisotropic homogeneous layered systems," *Phys. Rev. B*, vol. 53, p. 8, 1996.

[39] A. Dubroka, M. Rössle, K.W. Kim, et al., "Dynamical response and confinement of the electrons at the $LaAlO_3/SrTiO_3$ interface," *Phys. Rev. Lett.*, vol. 104, 2010, Art no. 156807.

[40] Z. M. Zhang, B. I. Choi, M. I. Flik, and A. C. Anderson, "Infrared refractive indices of $LaAlO_3$, $LaGaO_3$, and $NdGaO_3$," *J. Opt. Soc. Am. B*, vol. 11, p. 11, 1994.

[41] J. Humlicek and C. Bernhard, "Diffraction effects in infrared ellipsometry of conducting samples," *Thin Solid Films*, vol. 455–456, pp. 177–182, 2004.

[42] J. H. W. G. den Boer, G. M. W. Kroesen, M. Haverlag, and F. J. de Hoog, "Spectroscopic IR ellipsometry with imperfect components," *Thin Solid Films*, vol. 234, pp. 323–326, 1993.

[43] S. Kamba, E. Buixaderas, and A. Pajaczkowska, "Polarized infrared reflectivity spectra of $SrLaAlO_4$ and $SrLaGaO_4$ single crystals," *Phys. Status Solidi*, vol. 168, p. 317, 1998.

[44] J. Humlicek, R. Henn, and M. Cardona, "Infrared vibrations in $LaSrGaO_4$ and $LaSrAlO_4$," *Phys. Rev. B*, vol. 61, p. 21, 2000.

[45] T. N. Nunley, T. I. Willett-Gies, J. A. Cooke, et al., "Optical constants, band gap, and infrared-active phonons of $(LaAlO_3)_{0.3}(Sr_2AlTaO_6)_{0.35}$ (LSAT) from spectroscopic ellipsometry," *J. Vac. Sci. Technol., A*, vol. 34, 2016, Art. no. 051507.